Virtual testing of composites: imposing periodic boundary conditions on general finite element meshes

A. I. Akpoyomare[a,*], M. I. Okereke[a], M. S. Bingley[a]

[a] *Department of Engineering Science, University of Greenwich, Kent ME4 4TB, UK*

Abstract

Predicting the effective thermo-mechanical response of heterogeneous materials such as composites, using virtual testing techniques, requires imposing periodic boundary conditions on geometric domains. However, classic methods of imposing periodic boundary conditions require identical finite element mesh constructions on corresponding regions of geometric domains. This type of mesh construction is infeasible for heterogeneous materials with complex architecture such as textile composites where arbitrary mesh constructions are commonplace. This paper discusses interpolation technique for imposing periodic boundary conditions to arbitrary finite element mesh constructions (i.e. identical or non-identical meshes on corresponding regions of geometric domains), for predicting the effective properties of complex heterogeneous materials, using a through-thickness angle interlock textile composite as a test case. Furthermore, it espouses the implementation of the proposed periodic boundary condition enforcement technique in commercial finite element solvers. Benchmark virtual tests on identical and non-identical meshes demonstrate the high fidelity of the proposed periodic boundary condition enforcement technique, in comparison to the conventional technique of imposing periodic boundary condition and experimental data.

Keywords: Effective properties, Periodic boundary condition, Textile composite, Meso-scale modelling, Finite element, Heterogeneous materials, Virtual testing

1. Introduction

Virtual tests can reduce the cost of experimental testing in the aerospace industry by 50 % [1]. Furthermore, virtual testing techniques are precluded from the physical limitations of conventional experiments such as specimen size, testing conditions etc. [2]. Thus, virtual testing is suitable for characterising the entire intrinsic mechanical response of composites. Nevertheless, the predictive fidelity of virtual testing is determined chiefly by the accuracy of the geometric domain, material models and imposed boundary condition(s) (BC) [2]. In comparison with common BCs such

*Corresponding author
Email address: a.i.akpoyomare@gre.ac.uk (A. I. Akpoyomare)

as Dirchlet and Neumann BCs, periodic BC is the most efficient with respect to predictive accuracy, convergence rate and geometric domain size for virtual testing of heterogeneous materials [3, 4]. However, imposing periodic BC on textile geometric domains is arduous because the classic implementation method requires homologous finite element meshes at the boundaries of a geometric domain. This homologous mesh requirement is difficult to satisfy for textile composites because of their complex geometric topologies which yield non-homologous boundary mesh constructions [5, 6]; therefore arbitrary mesh constructions are the norm in virtual testing of textile composites. Thus, it is desirable to develop techniques for imposing periodic BC on arbitrary mesh constructions amenable to textile composites.

Nevertheless, some authors have devised techniques to generate homologous mesh construction on boundary surfaces of textiles. For example, Lomov and associates [5] used meshed shell structures to facilitate the generation of homologous meshes. Although, this technique requires a periodic geometric structure on boundary surfaces of the textile; thus it is inapplicable to a majority of textile structures. Other authors [7, 8] have adopted voxel mesh construction techniques to enforce a homologous mesh construction on boundary surfaces of textile composites. Voxel meshing, however, introduces numerical artefacts to geometric domains by virtue its discretisation process. These geometric artefacts inadvertently affect the predictive fidelity of such models. Thus, a more robust technique of imposing periodic BC to arbitrary conformal FE mesh constructions is necessary.

Jacques and co-workers [6] proposed a technique for imposing periodic BC to arbitrary textile meshes. Jacques and co-workers introduced several *reference nodes* in a Euclidean grid strructure which were kinematically coupled to existing nodes on corresponding surfaces on the textile RVE. However, the use of Laplacian spatial averaging to determine the location of these reference nodes violates the strict enforcement of spatial 'homologousness' between boundary surface pairs, which is a pre-requisite for PCBs. Thus, numerical artefacts can ensue from this anomaly which may become apparent in finite deformation regimes. Tyrus and associates [9] imposed periodic BC to arbitrary unidirectional (UD) composite meshes in 2D using polynomial interpolation techniques. The displacement fields of fibres and matrix were interpolated using linear and cubic interpolants, respectively. Recently, Nguyen and co-workers [4] generalised the technique of Tyrus and associates [9] and extended the formalisms to 3D cases of UD and particulate composites. The authors used Lagrange and piecewise cubic Hermite polynomial interpolants to determine the displacement fields along independent boundary edges. Displacement fields on RVE surfaces were interpolated using a bi-linear Coons patch formulation.

In this communication, we describe and implement a dual-scale homogenisation model for predicting the entire effective elastic properties of textile composites, using periodic BCs amenable to arbitrary textile meshes. We extend and implement a robust variant of the periodic BC method proposed by Nguyen and co-workers [4]. Furthermore, a method for implementing this technique in commercial FE solvers using conventional MPC equations is delineated, using ABAQUS's FE solver as a case study. Section 2 recalls the essentials of downscaling and describes the proposed periodic BC technique amenable to arbitrary meshes. Section 3 describes a method for its FE implementation in commercial FE solvers. In Section 5, the proposed periodic BC method is validated. Lastly, Section 6 describes the adopted virtual testing technique used to determine the entire effective elastic properties of textile composites.

2. Periodic Boundary Condition (PBC)

Consider a macroscopic continuum volume, $\Omega_{\text{continuum}}$, subjected to an arbitrary loading configuration as shown in Fig 1.

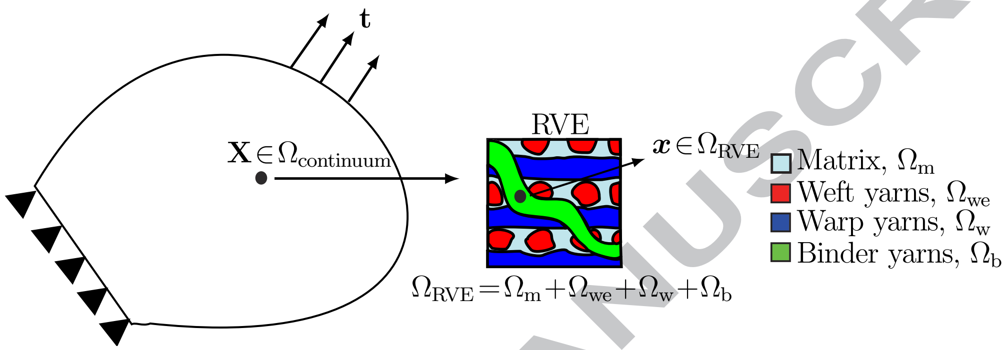

Figure 1: Schematic of isolation of an RVE domain, Ω_{RVE}, from an arbitrarily loaded macroscopic domain, $\Omega_{\text{continuum}}$.

Furthermore it is assumed that a local RVE volume, Ω_{RVE}, with boundary, $\partial\Omega_{\text{RVE}}$, is sufficiently resolved at a randomly sampled macroscopic material point, $\mathbf{X} \in \Omega_{\text{continuum}}$. In order to impose PBC on Ω_{RVE} in $\mathbb{R}^N$, where N is the dimensionality of the RVE's solution space, N, $\partial\Omega_{\text{RVE}}$ must consist of at least N pairs of faces. This is achieved by decomposing the entire boundary into two distinct parts: a positive part, $\partial\Omega^+_{\text{RVE}}$, and a negative part, $\partial\Omega^-_{\text{RVE}}$. Each corresponding pair of $\partial\Omega^+_{\text{RVE}}$ and $\partial\Omega^-_{\text{RVE}}$ have material points $\boldsymbol{x}^+$ and $\boldsymbol{x}^-$, respectively, such that, $\boldsymbol{x}^+ \in \partial\Omega^+_{\text{RVE}}$ and $\boldsymbol{x}^- \in \partial\Omega^-_{\text{RVE}}$. These have unit outward normals, $\boldsymbol{n}^+ = -\boldsymbol{n}^-$, respectively. Thus, the following relationship is satisfied

$$\partial\Omega^+_{\text{RVE}} \cup \partial\Omega^-_{\text{RVE}} = \partial\Omega_{\text{RVE}}. \tag{1}$$

Periodic BC is imposed on $\partial\Omega_{\text{RVE}}$ with the foregoing characteristics by enforcing periodicity of boundary fluctuation fields, $\tilde{\boldsymbol{u}}$, and anti-periodicity of boundary traction fields, $\boldsymbol{t}$, such that

$$(\forall \boldsymbol{x}^+ \in \partial\Omega^+_{\text{RVE}} \text{ and } \boldsymbol{x}^- \in \partial\Omega^-_{\text{RVE}}) \qquad \tilde{\boldsymbol{u}}(\boldsymbol{x}^+) = \tilde{\boldsymbol{u}}(\boldsymbol{x}^-), \tag{2}$$

$$(\forall \boldsymbol{x}^+ \in \partial\Omega^+_{\text{RVE}} \text{ and } \boldsymbol{x}^- \in \partial\Omega^-_{\text{RVE}}) \qquad \boldsymbol{t}(\boldsymbol{x}^+) = -\boldsymbol{t}(\boldsymbol{x}^-). \tag{3}$$

In practice two different types of FE mesh construction exists: a homologous mesh construction and a non-homologous mesh construction. Homologous FE meshes satisfy specific conditions such that

$$\#\partial\Omega^+_{\text{RVE}} = \#\partial\Omega^-_{\text{RVE}} \qquad \text{and} \tag{4}$$

$$(\forall \boldsymbol{x}^+ \in \partial\Omega^+_{\text{RVE}} \quad \text{and homologous } \boldsymbol{x}^- \in \partial\Omega^-_{\text{RVE}}) \qquad \boldsymbol{n}^+ \times \boldsymbol{n}^- = \mathbf{0}, \tag{5}$$

where # represents the cardinality of a set. Imposing PBC on homologous meshes is achieved by enforcing only Eqn (2) using classic methods that *kinematically tie* homologous boundary node pairs [3]. This kinematic tying is achieved using multi-point constraint equations [10]. Conversely, non-homologous FE meshes satisfy specific conditions such that

$$\#\partial\Omega^+_{\mathrm{RVE}} \stackrel{?}{=} \#\partial\Omega^-_{\mathrm{RVE}}, \qquad \text{and} \tag{6a}$$

$$(\exists \boldsymbol{x}^+ \in \partial\Omega^+_{\mathrm{RVE}} \text{ and } \boldsymbol{x}^- \in \partial\Omega^-_{\mathrm{RVE}}) \qquad \boldsymbol{n}^+ \times \boldsymbol{n}^- \neq \mathbf{0}. \tag{6b}$$

The conditions described by Eqn (6) are illustrated in Fig 2. In these cases, the classic *kinematic tying* of node pairs is unsuitable; therefore, more robust methods such as that proposed herein should be utilised.

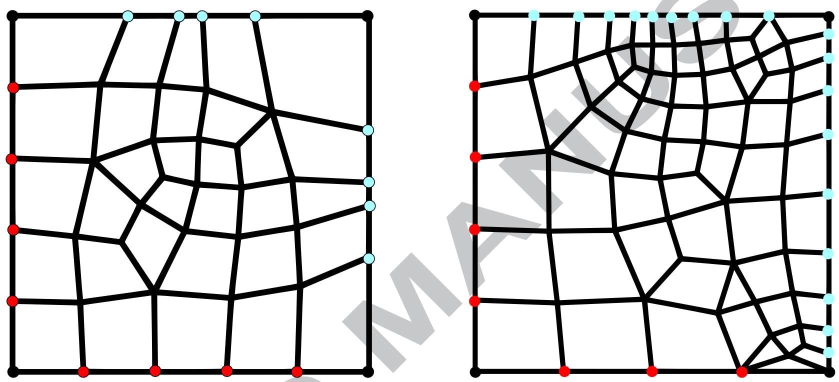

(a) (b)

Figure 2: Typical examples of non-homologous FE meshes in 2D (a) Eqn (6a), and (b) Eqn (6b). The red and light blue circles (●, ●) represents nodes on the -ve and +ve RVE boundaries, $\partial\Omega^-_{\mathrm{RVE}}$ and $\partial\Omega^+_{\mathrm{RVE}}$, respectively. The black circles (●) represents vertex nodes which are shared by $\partial\Omega^-_{\mathrm{RVE}}$ and $\partial\Omega^+_{\mathrm{RVE}}$.

2.1. Imposing PBC on Arbitrary FE Meshes

The underlying premise of the proposed periodic BC technique hinges on the proposition that the displacement field of $\partial\Omega_{\mathrm{RVE}}$ can be interpolated. Interpolation functions, $\mathbf{D}(\mathbf{s})$, are adopted such that Eqn (2) is satisfied. To this end, the following conditions are evoked to interpolate the displacement fields of the negative and positive parts of $\partial\Omega_{\mathrm{RVE}}$, respectively

$$\boldsymbol{u}(\mathbf{s})^- = \mathbf{D}(\mathbf{s}) = \sum_{k=1}^{n} \mathbf{N}_k(\mathbf{s})\boldsymbol{a}_k, \qquad \text{and} \tag{7}$$

$$\boldsymbol{u}(\mathbf{s})^+ = \mathbf{D}(\mathbf{s}) + \boldsymbol{\varepsilon}(\boldsymbol{x}^+ - \boldsymbol{x}^-), \tag{8}$$

where $\mathbf{N}_k(\mathbf{s})$ for $k \in \{k=1,2,\cdots,n\}$ are *shape functions* which solely depend on spatial variable(s), $\mathbf{s}$, $\boldsymbol{a}_k$ represents *independent variables*, $\boldsymbol{\varepsilon}$ is the strain tensor imposed at the continuum scale, and $(\boldsymbol{x}^+ - \boldsymbol{x}^-)$ depends of the RVE's dimensions. Therefore the displacement field of $\partial\Omega_{\mathrm{RVE}}$, is determined from the independent variables $\boldsymbol{a}_k$ and the applied far-field continuum scale strain $\boldsymbol{\varepsilon}$. The independent variables are selected as DOFs of specific nodes located at $\partial\Omega^-_{\mathrm{RVE}}$: these nodes are herein called *independent nodes.*.

In $\mathbb{R}^3$, Ω_{RVE} may be decomposed into edges and surfaces. Therefore, two different kinds of polynomial interpolants are necessary to interpolate Ω_{RVE} in $\mathbb{R}^3$: an edge interpolant and a surface interpolant. In principle, many univariate interpolation functions suffice for interpolating the displacement field of an RVE's edge; however, a piecewise cubic Hermite spline is adopted in this work because of its versatility [11]. Similarly, many bivariate interpolation functions suffice for interpolating the displacement field of an RVE's surface; however, a piecewise linear triangulation interpolation is adopted in this work because of its versatility [11]. These interpolants are discussed in Section 2.1.1 and Section 2.1.2, respectively.

2.1.1. Piecewise Cubic Hermite Interpolation for RVE Edges

To implement a piecewise cubic Hermite interpolant for an RVE's Edge, the edge is decomposed into n segments S_{i-1} for $i\in\{1,2,\cdots,n\}$ defined from $n+1$ triples $\{(\xi_0,\boldsymbol{u}_0,\boldsymbol{\theta}_0),\cdots,(\xi_n,\boldsymbol{u}_n,\boldsymbol{\theta}_n)\}$. Subsequently, the displacement field in each segment is interpolated using a third order Hermite polynomial:

$$
\begin{aligned}
H_1(\zeta) &= 1-3\zeta^2+2\zeta^3, && (9)\\
H_2(\zeta) &= l(\zeta-2\zeta^2+\zeta^3), && (10)\\
H_3(\zeta) &= 3\zeta^2-2\zeta^3, && (11)\\
H_4(\zeta) &= l(-\zeta^2+\zeta^3), && (12)
\end{aligned}
$$

where $\zeta(\xi)=\frac{\xi-\xi_{i-1}}{l}$, $l=\xi_i-\xi_{i-1}$ and $\xi_{i-1}\leqslant\xi\leqslant\xi_i$. Thus, the displacement field in each segment is represented as

$$\boldsymbol{u}(\xi)=H_1(\zeta(\xi))\boldsymbol{u}_{i-1}+H_2(\zeta(\xi))\boldsymbol{\theta}_{i-1}+H_3(\zeta(\xi))\boldsymbol{u}_i+H_4(\zeta(\xi))\boldsymbol{\theta}_i, \tag{13}$$

which can be written concisely in matrix form

$$\boldsymbol{u}(\xi)=\tilde{\mathbf{N}}\tilde{\boldsymbol{q}}, \tag{14}$$

where $\tilde{\mathbf{N}}$ is the local shape function matrix for the interpolant, and $\tilde{\boldsymbol{q}}=\left[\boldsymbol{u}_{i-1}^T\ \boldsymbol{\theta}_{i-1}^T\ \boldsymbol{u}_i^T\ \boldsymbol{\theta}_i^T\right]$ is the local vector of independent variables within each segment. Fig 3 shows a schematic representation of implementing the PBC interpolation technique for RVE edges using univariate polynomial interpolation functions.

2.1.2. Piecewise Linear Triangulation Interpolation for RVE Surfaces

To implement a piecewise linear triangulation interpolant for an RVE's surface, the surface is decomposed into a collection of n triangles T_i for $i\in\{1,2,\cdots,n\}$ which define a triangulation P. The number of triangles, n, in the triangulation, P, is defined as $n=2k-b-2$, where k is the number of points in P and b is the number of points in P that lie on the boundary of the convex hull of P.

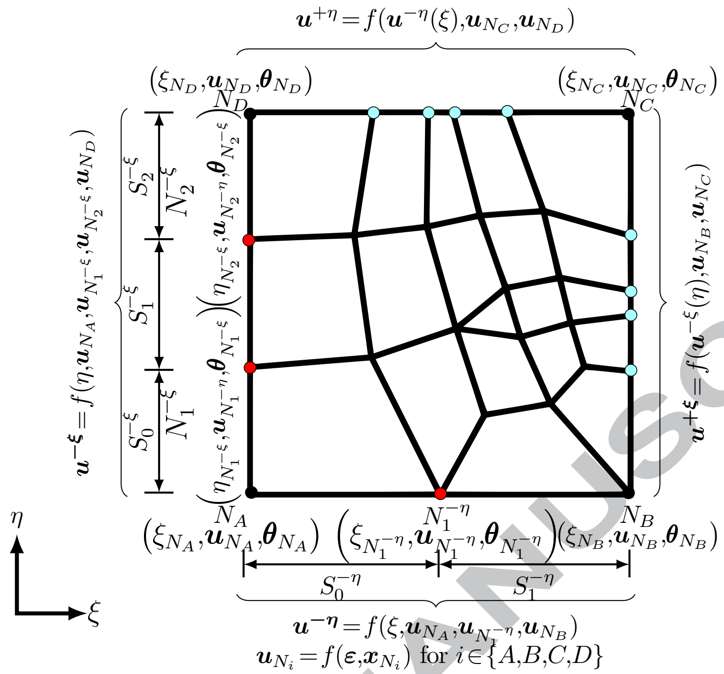

Figure 3: Schematic showing the implementation of PBC interpolation technique for RVE edges using univariate polynomial interpolation functions where $\boldsymbol{u}$ represents a displacement field, $\boldsymbol{\varepsilon}$ represents the macroscopic strain tensor and $\boldsymbol{x}_{\boldsymbol{N_i}}$ represents a material point of node N_i for $i \in \{A,B,C,D\}$.

Many different triangulation techniques may be used to decompose the RVE's surface [11]. This work adopts a Delaunay triangulation because it produces optimally shaped triangles which are necessary for good interpolation [11]. Subsequently, the displacement field within each triangle, with vertices v_1, v_2 and v_3, is interpolated using a linear barycentric polynomial:

$$B_1(\xi,\eta) = \frac{\text{area}(v(\xi,\eta), v_2(\xi,\eta), v_3(\xi,\eta))}{\text{area}(v_1(\xi,\eta), v_2(\xi,\eta), v_3(\xi,\eta))}, \tag{15}$$

$$B_2(\xi,\eta) = \frac{\text{area}(v(\xi,\eta), v_1(\xi,\eta), v_3(\xi,\eta))}{\text{area}(v_1(\xi,\eta), v_2(\xi,\eta), v_3(\xi,\eta))}, \tag{16}$$

$$B_3(\xi,\eta) = \frac{\text{area}(v(\xi,\eta), v_1(\xi,\eta), v_2(\xi,\eta))}{\text{area}(v_1(\xi,\eta), v_2(\xi,\eta), v_3(\xi,\eta))}, \tag{17}$$

where $B_1 + B_2 + B_3 = 1$. Thus, the displacement field within each triangle is represented as

$$\boldsymbol{u}(\xi,\eta) = B_1(\xi,\eta)\boldsymbol{u}_{v_1} + B_2(\xi,\eta)\boldsymbol{u}_{v_2} + B_3(\xi,\eta)\boldsymbol{u}_{v_3}, \tag{18}$$

which can be written concisely in matrix form

$$\boldsymbol{u}(\xi,\eta) = \tilde{\mathbf{N}}\tilde{\boldsymbol{q}}, \tag{19}$$

where $\tilde{\mathbf{N}}$ is the local shape function matrix for the interpolant, and $\tilde{\boldsymbol{q}} = [\boldsymbol{u}_{v_1}\ \boldsymbol{u}_{v_2}\ \boldsymbol{u}_{v_3}]$ is the local vector of independent variables within each triangle. Fig 4 shows a schematic representation of implementing the PBC interpolation technique for RVE surfaces using piecewise linear triangulation interpolation functions.

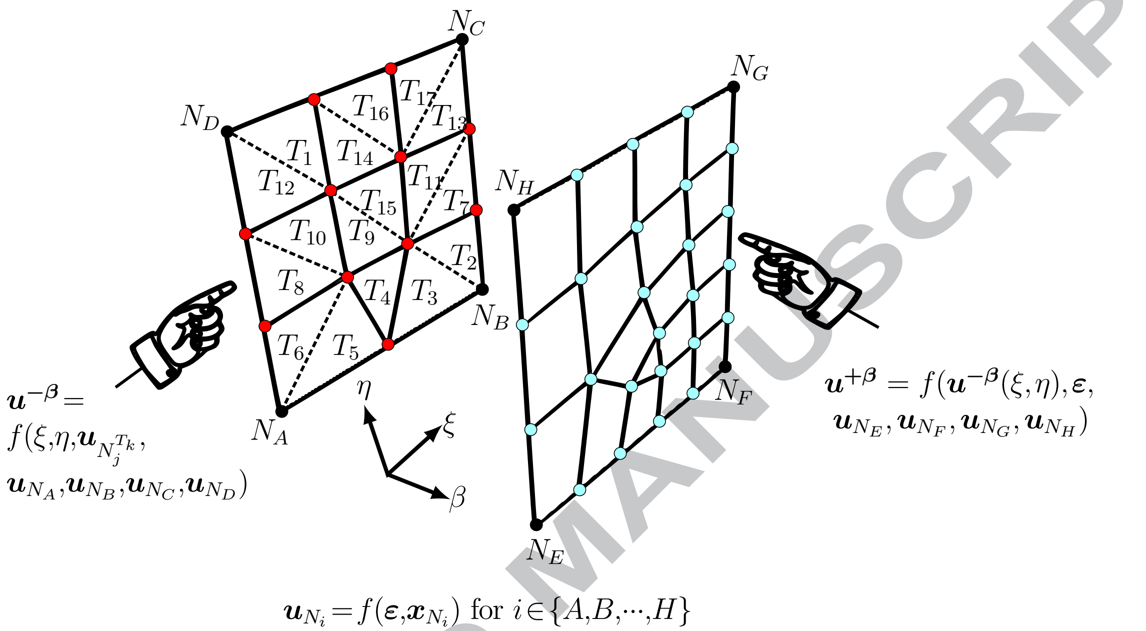

Figure 4: Schematic showing the implementation of PBC interpolation technique for RVE surfaces using piecewise linear triangulation interpolation functions. Note that $\boldsymbol{u}$ represents a displacement field, $\boldsymbol{\varepsilon}$ represents the macroscopic strain tensor, $\boldsymbol{x}_{\boldsymbol{N_i}}$ represents a material point of node N_i for $i \in \{A, B, \cdots, H\}$ and $\boldsymbol{u}_{N_j^{T_k}}$ represents the displacement field of node N_j in triangle T_k for $i \in \{1,2,3\}$ and $k \in \{1,2,\cdots,17\}$.

3. FE implementation of PBC Enforcement for Arbitrary Meshes

Directly implementing Eqns (8), (14) and (19) in $\mathbb{R}^3$ within commercial FE solvers presents two major challenges. First, the dependent nodes shared by two or more faces (i.e. edge and vertex nodes) are over-constrained because each node has uniquely defined DOFs which must not be specified more than once. Therefore, the constraint equations for these shared nodal sets must be treated carefully. This requires proper decomposition of nodal sets on, $\partial\Omega_{\text{RVE}}$, to preclude repetition. Second, the independent 'rotation' terms in the Hermite shape functions and the $\boldsymbol{\varepsilon}$ are naturally inaccessible in the FE problem. These inaccessible DOFs are introduced to the FE problem as additional DOFs using *supplementary nodes*.

3.1. Decomposition of RVE domain $\partial\Omega_{RVE}$

Consider $\partial\Omega_{\text{RVE}}$ of a parallelepiped in $\mathbb{R}^3$ to be imposed with PBC as shown in Fig 5. The YZ plane located at the minimum X dimension represents the negative X-axis boundary, $\partial\Omega_{\text{RVE}}^{X-}$.

Similarly, the YZ plane located at the maximum X dimension represents the positive X-axis boundary, $\partial\Omega^{X+}_{\mathrm{RVE}}$. Similar arguments apply for the other surfaces of the RVE as shown in Fig 5. The aforementioned surfaces of the RVE's boundary are decomposed further into a set of vertex, edge and internal surface regions.

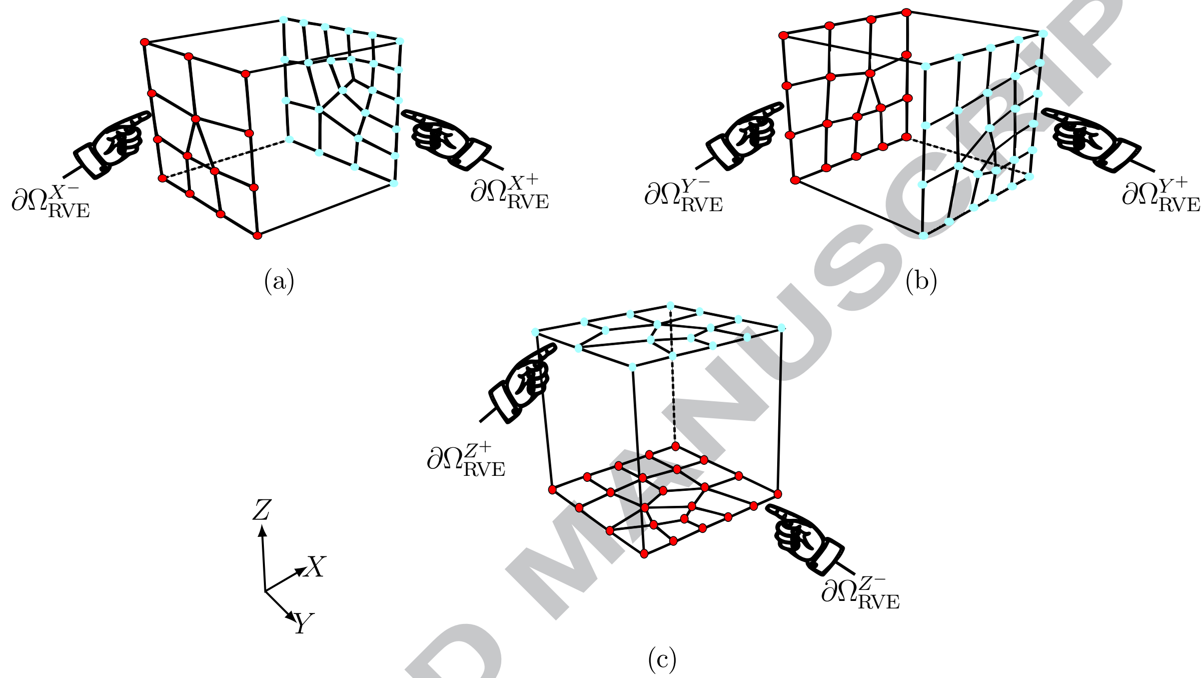

Figure 5: Schematic of nodal decomposition of $\partial\Omega_{\mathrm{RVE}}$, in $\mathbb{R}^3$ (a) $\partial\Omega^{X-}_{\mathrm{RVE}}$ and $\partial\Omega^{X+}_{\mathrm{RVE}}$, (b) $\partial\Omega^{Y-}_{\mathrm{RVE}}$ and $\partial\Omega^{Y+}_{\mathrm{RVE}}$, and (c) $\partial\Omega^{Z-}_{\mathrm{RVE}}$ and $\partial\Omega^{Z+}_{\mathrm{RVE}}$.

3.1.1. Identification of RVE vertex regions

Vertex regions of the RVE are shared by three mutually perpendicular surfaces and are isolated as follows

$$
\begin{aligned}
\partial\Omega^{X-Y-Z-}_{\mathrm{RVE}} &= \partial\Omega^{X-}_{\mathrm{RVE}} \cap \partial\Omega^{Y-}_{\mathrm{RVE}} \cap \partial\Omega^{Z-}_{\mathrm{RVE}},\\
\partial\Omega^{X+Y-Z-}_{\mathrm{RVE}} &= \partial\Omega^{X+}_{\mathrm{RVE}} \cap \partial\Omega^{Y-}_{\mathrm{RVE}} \cap \partial\Omega^{Z-}_{\mathrm{RVE}},\\
&\vdots\\
\partial\Omega^{X-Y+Z+}_{\mathrm{RVE}} &= \partial\Omega^{X-}_{\mathrm{RVE}} \cap \partial\Omega^{Y+}_{\mathrm{RVE}} \cap \partial\Omega^{Z+}_{\mathrm{RVE}}.
\end{aligned}
\tag{20}
$$

The vertex regions defined in Eqn (20) are depicted schematically in Fig 6.

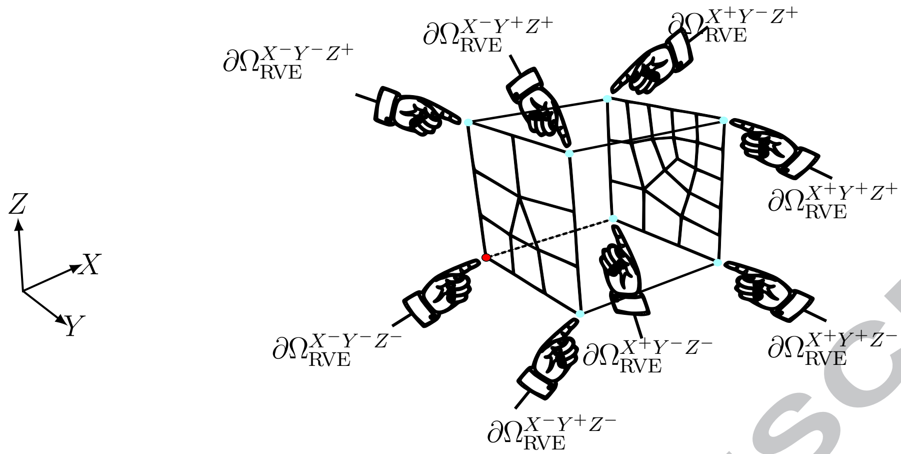

Figure 6: Isolation of 8 vertex regions, $\partial\Omega_{\mathrm{RVE}}^{X^-Y^-Z^-}$, $\partial\Omega_{\mathrm{RVE}}^{X^+Y^-Z^-}$, $\partial\Omega_{\mathrm{RVE}}^{X^+Y^+Z^-}$, $\partial\Omega_{\mathrm{RVE}}^{X^-Y^+Z^-}$, $\partial\Omega_{\mathrm{RVE}}^{X^-Y^-Z^+}$, $\partial\Omega_{\mathrm{RVE}}^{X^+Y^-Z^+}$,$\partial\Omega_{\mathrm{RVE}}^{X^+Y^+Z^+}$,$\partial\Omega_{\mathrm{RVE}}^{X^-Y^+Z^+}$, on $\partial\Omega_{\mathrm{RVE}}$.

3.1.2. Identification of RVE edge regions

Independent edge regions of $\partial\Omega_{\mathrm{RVE}}$, shared by two mutually perpendicular faces, are isolated as follows

$$
\begin{aligned}
\partial\Omega_{\mathrm{RVE}}^{Y^-Z^-} &= \left(\partial\Omega_{\mathrm{RVE}}^{Y^-} \cap \partial\Omega_{\mathrm{RVE}}^{Z^-}\right) \setminus \left(\partial\Omega_{\mathrm{RVE}}^{X^-Y^-Z^-} \cup \partial\Omega_{\mathrm{RVE}}^{X^+Y^-Z^-}\right),\\
\partial\Omega_{\mathrm{RVE}}^{Y^+Z^-} &= \left(\partial\Omega_{\mathrm{RVE}}^{Y^+} \cap \partial\Omega_{\mathrm{RVE}}^{Z^-}\right) \setminus \left(\partial\Omega_{\mathrm{RVE}}^{X^-Y^+Z^-} \cup \partial\Omega_{\mathrm{RVE}}^{X^+Y^+Z^-}\right),\\
&\ \vdots\\
\partial\Omega_{\mathrm{RVE}}^{X^+Y^-} &= \left(\partial\Omega_{\mathrm{RVE}}^{X^+} \cap \partial\Omega_{\mathrm{RVE}}^{Y^-}\right) \setminus \left(\partial\Omega_{\mathrm{RVE}}^{X^+Y^-Z^-} \cup \partial\Omega_{\mathrm{RVE}}^{X^+Y^-Z^+}\right).
\end{aligned}
\tag{21}
$$

The edge regions defined in Eqn (21) are depicted schematically in Fig 7.

3.1.3. Identification internal surface regions on $\partial\Omega_{RVE}$

Internal surface regions on $\partial\Omega_{\mathrm{RVE}}$ are isolated as follows

$$
\begin{aligned}
\partial\Omega_{\mathrm{RVE}}^{X^-\mathrm{int}} &= \partial\Omega_{\mathrm{RVE}}^{X^-} \setminus \left(\partial\Omega_{\mathrm{RVE}}^{Y^-} \cup \partial\Omega_{\mathrm{RVE}}^{Y^+} \cup \partial\Omega_{\mathrm{RVE}}^{Z^-} \cup \partial\Omega_{\mathrm{RVE}}^{Z^+}\right),\\
\partial\Omega_{\mathrm{RVE}}^{X^+\mathrm{int}} &= \partial\Omega_{\mathrm{RVE}}^{X^+} \setminus \left(\partial\Omega_{\mathrm{RVE}}^{Y^-} \cup \partial\Omega_{\mathrm{RVE}}^{Y^+} \cup \partial\Omega_{\mathrm{RVE}}^{Z^-} \cup \partial\Omega_{\mathrm{RVE}}^{Z^+}\right),\\
&\ \vdots\\
\partial\Omega_{\mathrm{RVE}}^{Z^+\mathrm{int}} &= \partial\Omega_{\mathrm{RVE}}^{Z^+} \setminus \left(\partial\Omega_{\mathrm{RVE}}^{X^-} \cup \partial\Omega_{\mathrm{RVE}}^{X^+} \cup \partial\Omega_{\mathrm{RVE}}^{Y^-} \cup \partial\Omega_{\mathrm{RVE}}^{Y^+}\right).
\end{aligned}
\tag{22}
$$

The internal surface regions defined in Eqn (22) are depicted schematically in Fig 8.

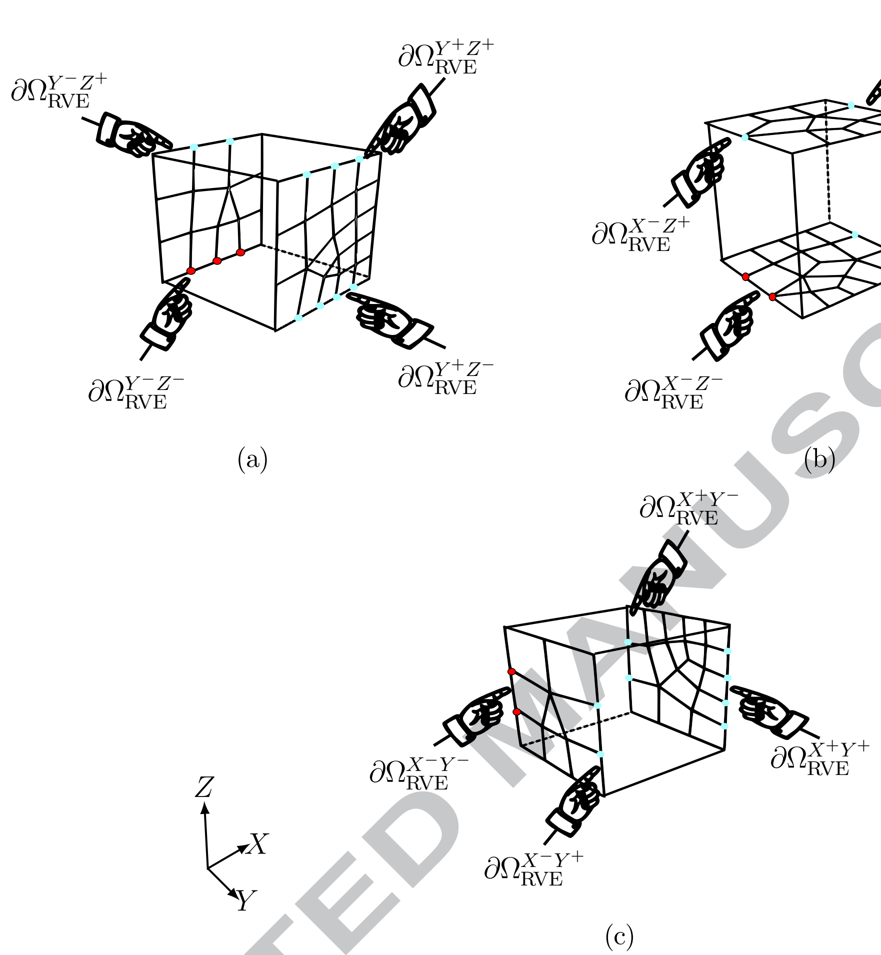

Figure 7: Isolation of 12 RVE edge regions; edges aligned along the principal (a) $X-$ direction: $\partial\Omega_{\mathrm{RVE}}^{Y^-Z^-}$ $\partial\Omega_{\mathrm{RVE}}^{Y^+Z^-}$ $\partial\Omega_{\mathrm{RVE}}^{Y^+Z^+}$, and $\partial\Omega_{\mathrm{RVE}}^{Y^-Z^+}$ (b) $Y-$ direction: $\partial\Omega_{\mathrm{RVE}}^{X^-Z^-}$ $\partial\Omega_{\mathrm{RVE}}^{X^+Z^-}$ $\partial\Omega_{\mathrm{RVE}}^{X^+Z^+}$ and $\partial\Omega_{\mathrm{RVE}}^{X^-Z^+}$, and (c) $Z-$ direction: $\partial\Omega_{\mathrm{RVE}}^{X^-Y^-}$ $\partial\Omega_{\mathrm{RVE}}^{X^-Y^+}$ $\partial\Omega_{\mathrm{RVE}}^{X^+Y^+}$ and $\partial\Omega_{\mathrm{RVE}}^{X^+Y^-}$.

Eqns (20)–(22) ensure that no decomposed boundary region is a proper subset of another; thus, eliminating the possibility of over-constraining $\partial\Omega_{\mathrm{RVE}}$.

3.2. Identification of independent vertex, edge and internal surface regions on $\partial\Omega_{RVE}$

Having decomposed $\partial\Omega_{\mathrm{RVE}}$, proper enforcement of PBC to requires the definition of two distinct sets of boundary regions: independent and dependent regions, respectively. Dependent regions are obtained by translational symmetry of independent regions. In this work, regions comprising $\partial\Omega^-_{\mathrm{RVE}}$ are regarded independent regions. Furthermore, to prevent over-constraint of regions mutually present in $\partial\Omega^-_{\mathrm{RVE}}$ and $\partial\Omega^+_{\mathrm{RVE}}$, only a subset of $\partial\Omega^-_{\mathrm{RVE}}$ are considered an independent. Considering $\partial\Omega_{\mathrm{RVE}}$ in Fig 5, a region is considered independent $\Leftrightarrow$ $\partial\Omega^-_{\mathrm{RVE}} \cap \partial\Omega^+_{\mathrm{RVE}} = \varnothing$. Thus, in honouring this condition, independent node, edge and surface regions of this RVE are shown in Figs 6–8.

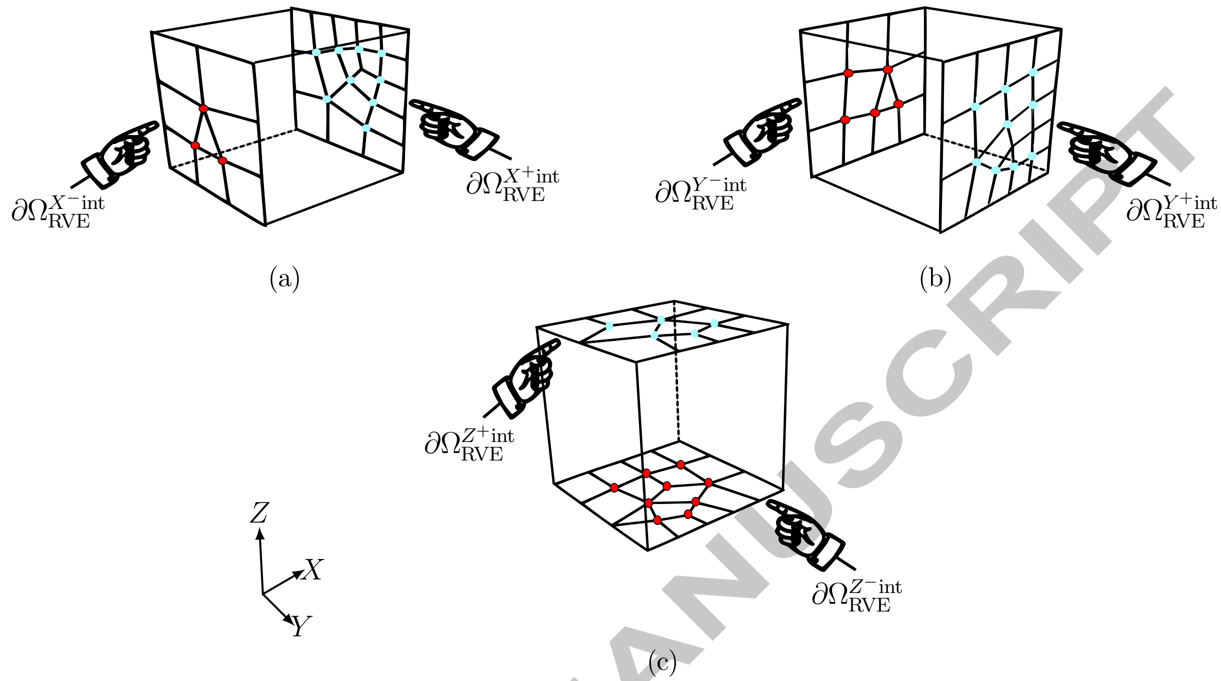

Figure 8: Isolation of 6 RVE internal surfaces regions, (a) internal X surfaces regions corresponding to $\partial\Omega_{\mathrm{RVE}}^{X^{-}\mathrm{int}}$ and $\partial\Omega_{\mathrm{RVE}}^{X^{+}\mathrm{int}}$, (b) internal Y surfaces regions corresponding to $\partial\Omega_{\mathrm{RVE}}^{Y^{-}}$ and $\partial\Omega_{\mathrm{RVE}}^{Y^{+}}$, and (c) internal Z surfaces regions corresponding to $\partial\Omega_{\mathrm{RVE}}^{Z^{-}}$ and $\partial\Omega_{\mathrm{RVE}}^{Z^{+}}$.

3.3. Application of multi-point constraint equation to the RVE domain $\partial\Omega_{RVE}$

The segregation of independent and dependent boundary regions of the RVE, performed in the preceding paragraph, permits the proper implementation of periodic BC on the RVE without over constraints. In practice, the periodic BC given in Eqns (8), (14) and (19) represent non-homogeneous linear multi-point constraints (MPCs). The canonical form of representing these MPCs in FE solvers is

$$A_1 u_i^{\mathrm{A}} + \hat{A}_1 \hat{u}_i^{\hat{\mathrm{A}}} + A_2 u_j^{\mathrm{B}} + \hat{A}_2 \hat{u}_j^{\hat{\mathrm{B}}} + \cdots + A_N u_k^{\mathrm{R}} + \hat{A}_M \hat{u}_j^{\hat{\mathrm{R}}} = 0, \tag{23}$$

where u_k^{R} represents the FE nodal variable (e.g. displacement) at node R, degree of freedom i, and the coefficient A_N determines the relative magnitude of contribution from its conjugate nodal variable to the constraint equation, for $i,j,k \in \{1,2,3\}$. The terms with hats '$\hat{\ }$' in Eqn (23) are associated with *supplementary nodes* introduced into the FE problem. These supplementary nodes are not attached to any element within the original model being analysed but are only introduced to facilitate implementation of the constrain equations. Therefore, the nodal variable of these supplementary nodes can be used to introduce the independent rotation terms in the Hermite shape functions and the continuum strain tensor components; for example, $\hat{\boldsymbol{u}} \equiv \boldsymbol{\theta}$ or $\hat{\boldsymbol{u}} \equiv \boldsymbol{\epsilon}$.

Considering Eqns (8), (14) and (19) with respect to Eqn (23), the sets of MPCs the enforce the periodic BC to the cubical/parallelipipied RVE with an arbitrary FE mesh are

$$
\begin{aligned}
u_i^{\partial\Omega_{\mathrm{RVE}}^{X^+Y^-Z^-}} - u_i^{\partial\Omega_{\mathrm{RVE}}^{X^-Y^-Z^-}} &- (x_j^{\partial\Omega_{\mathrm{RVE}}^{X^+Y^-Z^-}} - x_j^{\partial\Omega_{\mathrm{RVE}}^{X^-Y^-Z^-}})\hat{u}_j^{\hat{\epsilon}^i} = 0,\\
u_i^{\partial\Omega_{\mathrm{RVE}}^{X^+Y^+Z^-}} - u_i^{\partial\Omega_{\mathrm{RVE}}^{X^-Y^-Z^-}} &- (x_j^{\partial\Omega_{\mathrm{RVE}}^{X^+Y^+Z^-}} - x_j^{\partial\Omega_{\mathrm{RVE}}^{X^-Y^-Z^-}})\hat{u}_j^{\hat{\epsilon}^i} = 0,\\
u_i^{\partial\Omega_{\mathrm{RVE}}^{X^-Y^+Z^-}} - u_i^{\partial\Omega_{\mathrm{RVE}}^{X^-Y^-Z^-}} &- (x_j^{\partial\Omega_{\mathrm{RVE}}^{X^-Y^+Z^-}} - x_j^{\partial\Omega_{\mathrm{RVE}}^{X^-Y^-Z^-}})\hat{u}_j^{\hat{\epsilon}^i} = 0,\\
u_i^{\partial\Omega_{\mathrm{RVE}}^{X^-Y^-Z^+}} - u_i^{\partial\Omega_{\mathrm{RVE}}^{X^-Y^-Z^-}} &- (x_j^{\partial\Omega_{\mathrm{RVE}}^{X^-Y^-Z^+}} - x_j^{\partial\Omega_{\mathrm{RVE}}^{X^-Y^-Z^-}})\hat{u}_j^{\hat{\epsilon}^i} = 0,\\
u_i^{\partial\Omega_{\mathrm{RVE}}^{X^+Y^-Z^+}} - u_i^{\partial\Omega_{\mathrm{RVE}}^{X^-Y^-Z^-}} &- (x_j^{\partial\Omega_{\mathrm{RVE}}^{X^+Y^-Z^+}} - x_j^{\partial\Omega_{\mathrm{RVE}}^{X^-Y^-Z^-}})\hat{u}_j^{\hat{\epsilon}^i} = 0,\\
u_i^{\partial\Omega_{\mathrm{RVE}}^{X^+Y^+Z^+}} - u_i^{\partial\Omega_{\mathrm{RVE}}^{X^-Y^-Z^-}} &- (x_j^{\partial\Omega_{\mathrm{RVE}}^{X^+Y^+Z^+}} - x_j^{\partial\Omega_{\mathrm{RVE}}^{X^-Y^-Z^-}})\hat{u}_j^{\hat{\epsilon}^i} = 0,\\
u_i^{\partial\Omega_{\mathrm{RVE}}^{X^-Y^+Z^+}} - u_i^{\partial\Omega_{\mathrm{RVE}}^{X^-Y^-Z^-}} &- (x_j^{\partial\Omega_{\mathrm{RVE}}^{X^-Y^+Z^+}} - x_j^{\partial\Omega_{\mathrm{RVE}}^{X^-Y^-Z^-}})\hat{u}_j^{\hat{\epsilon}^i} = 0,\\
u_i^{\partial\Omega_{\mathrm{RVE}}^{X^-Y^-Z^-}} &- x_j^{\partial\Omega_{\mathrm{RVE}}^{X^-Y^-Z^-}} \hat{u}_j^{\hat{\epsilon}^i} = 0,\\
u_i^{\partial\Omega_{\mathrm{RVE}}^{Y^+Z^-}} - u_i^{\partial\Omega_{\mathrm{RVE}}^{Y^-Z^-}} &- (x_j^{\partial\Omega_{\mathrm{RVE}}^{X^-Y^+Z^-}} - x_j^{\partial\Omega_{\mathrm{RVE}}^{X^-Y^-Z^-}})\hat{u}_j^{\hat{\epsilon}^i} = 0,\\
u_i^{\partial\Omega_{\mathrm{RVE}}^{Y^+Z^+}} - u_i^{\partial\Omega_{\mathrm{RVE}}^{Y^-Z^-}} &- (x_j^{\partial\Omega_{\mathrm{RVE}}^{X^-Y^+Z^+}} - x_j^{\partial\Omega_{\mathrm{RVE}}^{X^-Y^-Z^-}})\hat{u}_j^{\hat{\epsilon}^i} = 0,\\
u_i^{\partial\Omega_{\mathrm{RVE}}^{Y^-Z^+}} - u_i^{\partial\Omega_{\mathrm{RVE}}^{Y^-Z^-}} &- (x_j^{\partial\Omega_{\mathrm{RVE}}^{X^-Y^-Z^+}} - x_j^{\partial\Omega_{\mathrm{RVE}}^{X^-Y^-Z^-}})\hat{u}_j^{\hat{\epsilon}^i} = 0,\\
u_i^{\partial\Omega_{\mathrm{RVE}}^{X^+Z^-}} - u_i^{\partial\Omega_{\mathrm{RVE}}^{X^-Z^-}} &- (x_j^{\partial\Omega_{\mathrm{RVE}}^{X^+Y^-Z^-}} - x_j^{\partial\Omega_{\mathrm{RVE}}^{X^-Y^-Z^-}})\hat{u}_j^{\hat{\epsilon}^i} = 0,\\
u_i^{\partial\Omega_{\mathrm{RVE}}^{X^+Z^+}} - u_i^{\partial\Omega_{\mathrm{RVE}}^{X^-Z^-}} &- (x_j^{\partial\Omega_{\mathrm{RVE}}^{X^+Y^-Z^+}} - x_j^{\partial\Omega_{\mathrm{RVE}}^{X^-Y^-Z^-}})\hat{u}_j^{\hat{\epsilon}^i} = 0,\\
u_i^{\partial\Omega_{\mathrm{RVE}}^{X^-Z^+}} - u_i^{\partial\Omega_{\mathrm{RVE}}^{X^-Z^-}} &- (x_j^{\partial\Omega_{\mathrm{RVE}}^{X^-Y^-Z^+}} - x_j^{\partial\Omega_{\mathrm{RVE}}^{X^-Y^-Z^-}})\hat{u}_j^{\hat{\epsilon}^i} = 0,\\
u_i^{\partial\Omega_{\mathrm{RVE}}^{X^-Y^+}} - u_i^{\partial\Omega_{\mathrm{RVE}}^{X^-Y^-}} &- (x_j^{\partial\Omega_{\mathrm{RVE}}^{X^-Y^+Z^-}} - x_j^{\partial\Omega_{\mathrm{RVE}}^{X^-Y^-Z^-}})\hat{u}_j^{\hat{\epsilon}^i} = 0,\\
u_i^{\partial\Omega_{\mathrm{RVE}}^{X^+Y^+}} - u_i^{\partial\Omega_{\mathrm{RVE}}^{X^-Z^-}} &- (x_j^{\partial\Omega_{\mathrm{RVE}}^{X^+Y^+Z^-}} - x_j^{\partial\Omega_{\mathrm{RVE}}^{X^-Y^-Z^-}})\hat{u}_j^{\hat{\epsilon}^i} = 0,\\
u_i^{\partial\Omega_{\mathrm{RVE}}^{X^+Y^-}} - u_i^{\partial\Omega_{\mathrm{RVE}}^{X^-Y^-}} &- (x_j^{\partial\Omega_{\mathrm{RVE}}^{X^+Y^-Z^-}} - x_j^{\partial\Omega_{\mathrm{RVE}}^{X^-Y^-Z^-}})\hat{u}_j^{\hat{\epsilon}^i} = 0,\\
u_i^{\partial\Omega_{\mathrm{RVE}}^{X^+\mathrm{int}}} - u_i^{\partial\Omega_{\mathrm{RVE}}^{X^-\mathrm{int}}} &- (x_j^{\partial\Omega_{\mathrm{RVE}}^{X^+Y^-Z^-}} - x_j^{\partial\Omega_{\mathrm{RVE}}^{X^-Y^-Z^-}})\hat{u}_j^{\hat{\epsilon}^i} = 0,\\
u_i^{\partial\Omega_{\mathrm{RVE}}^{Y^+\mathrm{int}}} - u_i^{\partial\Omega_{\mathrm{RVE}}^{Y^-\mathrm{int}}} &- (x_j^{\partial\Omega_{\mathrm{RVE}}^{X^-Y^+Z^-}} - x_j^{\partial\Omega_{\mathrm{RVE}}^{X^-Y^-Z^-}})\hat{u}_j^{\hat{\epsilon}^i} = 0,\\
u_i^{\partial\Omega_{\mathrm{RVE}}^{Z^+\mathrm{int}}} - u_i^{\partial\Omega_{\mathrm{RVE}}^{Z^-\mathrm{int}}} &- (x_j^{\partial\Omega_{\mathrm{RVE}}^{X^-Y^-Z^+}} - x_j^{\partial\Omega_{\mathrm{RVE}}^{X^-Y^-Z^-}})\hat{u}_j^{\hat{\epsilon}^i} = 0,
\end{aligned}
\tag{24}
$$

where $\hat{\epsilon}^i$ for $i \in \{1,2,3\}$ represents supplementary nodes which are used to enforce the continuum strain tensor on the RVE.

4. Computational Homogenisation

Computational homogenisation is used to bridge $\Omega_{\text{continuum}}$ and Ω_{RVE}. The principal aim is to obtain the continuum scale Cauchy stress, $\boldsymbol{\sigma}$ from an imposed continuum strain $\boldsymbol{\epsilon}$. Consequently, continuum scale parameters such as effective elastic constants are obtained thereafter. It is assumed that Ω_{RVE} is in equilibrium such that

$$\frac{\partial \sigma_{ij}}{\partial x_j} = 0 \qquad \forall \boldsymbol{x} \in \Omega_{\text{RVE}}, \qquad \text{and} \tag{25}$$

$$\sigma_{ij} n_j = \bar{t}_i \qquad \forall \boldsymbol{x} \in \partial\Omega_{\text{RVE}}. \tag{26}$$

Based on classical averaging theory, σ_{ij}, and ϵ_{ij}, are defined as the volume average of the corresponding RVE scale stresses, $\overline{\sigma}_{ij}$, and strains, $\overline{\epsilon}_{ij}$, given by

$$\sigma_{ij} = \frac{1}{V} \int_{\Omega_{\text{RVE}}} \overline{\sigma}_{ij} \mathrm{d}V, \qquad \text{and} \tag{27}$$

$$\epsilon_{ij} = \frac{1}{V} \int_{\Omega_{\text{RVE}}} \overline{\epsilon}_{ij} \mathrm{d}V. \tag{28}$$

The principle of virtual work to homogenise the response of Ω_{RVE} is given by [12]

$$\delta W_{\text{ext}} + \delta W_{\text{int}} = 0, \tag{29}$$

where, δW_{ext} is the virtual external work performed by external loads on Ω_{RVE} and δW_{int} is the virtual internal work performed by the average Cauchy stresses within Ω_{RVE}. The external virtual work can be expressed as

$$\delta W_{\text{ext}} = \oint_{\partial\Omega_{\text{RVE}}} \overline{\sigma}_{ik} n_k \delta u_i \mathrm{d}S = \oint_{\partial\Omega_{\text{RVE}}} \bar{t}_i \delta u_i \mathrm{d}S, \tag{30}$$

where δu_i represents a virtual displacement in the i direction. The Cauchy stress is work conjugate to true strain, hence the internal virtual work is expressed as

$$\delta W_{\text{int}} = -V \sigma_{ij} \delta \epsilon_{ij}. \tag{31}$$

Combining Eqns (29)–(31) yields

$$\oint_{\partial\Omega_{\text{RVE}}} \bar{t}_i \delta u_i \mathrm{d}S = V \sigma_{ij} \delta \epsilon_{ij}. \tag{32}$$

In this work, the components continuum scale strain tensor, which drive the deformation of the RVE, are introduced via the nine degrees of freedom of the supplementary nodes, $\hat{\epsilon}^i$, such that

$$\hat{u}_j^{\hat{\epsilon}^i} = \epsilon_{ij}. \tag{33}$$

Therefore, the external virtual work can be in terms of the degrees of freedom of the supplementary nodes, and their work conjugate forces, Υ^i_j , such that,

$$\delta W_{\text{ext}} = \hat{\Upsilon}^i_j \delta \hat{u}^{\hat{\epsilon} i}_j, \tag{34}$$

where Υ^i_j is the reaction force of supplementary node i at degree of freedom j corresponding to its assigned displacements. Using Eqns (31) and (34), the macroscopic Cauchy stress becomes

$$\sigma_{ij} = \frac{\hat{\Upsilon}^i_j}{V}. \tag{35}$$

To predict the effective elastic properties at $\Omega_{\text{continuum}}$, the relationship between the stresses and strains for an orthotropic material is given by

$$\epsilon_{ij} = S_{ijkl} \sigma_{ij}, \tag{36}$$

where S_{ijkl} represents the compliance of the material from which its effective elastic constants are retrieved [3].

5. Validation of PBC Enforcement for Arbitrary Finite Element Meshes

Evaluating the robustness of the proposed PBC enforcement technique necessitates a comparison between predictions obtained from its implementation and the classic PBC enforcement by kinematic tying of nodal pairs [3]. For the purpose of comparison with PBC enforcement by kinematic tying, a homologous RVE mesh was considered. However, for the case of a non-homologous mesh, only the proposed PBC enforcement using polynomial interpolation was amenable (see Fig 9). For this validation analysis, we adopt a unidirectional (UD) composite. In this validation exercise, a UD composite was selected because the FE mesh generation of such RVE's can be easily controlled to produce homologous or non-homologous Besides, since the proposed technique is applicable to general FE mesh constructions, the validity of the technique can be scrutinised for both homologous and non-homologous mesh constructions.

5.1. Test material for PBC validation

The selected test material for the validation analysis is a carbon fibre-reinforced epoxy composite (T300/BSL914C) with a 60 % fibre volume fraction (i.e. $V_f = 60\%$), used in the world-wide failure exercise [13]. This composite was chosen because experimental data on eight, out of the nine independent effective elastic properties, were available. The properties of constituents comprising T300/BSL914C are reported in Tab 1.

Table 1: Mechanical properties of constituents comprising T300/BSL914C with $V_f = 60\%$ [13].

Elastic constant	Fibre (T300)	Matrix (BSL914C)
Longitudinal modulus (GPa), E_{11}	230	4
Transverse modulus (GPa), E_{22}	3.45	4
In-plane shear modulus (GPa), G_{12}	15	1.481
Transverse shear modulus (GPa), G_{23}	7	1.481
Major Poisson's ratio, ν_{12}	0.2	0.35

5.2. Geometric model generation and set-up

The spatial morphology of fibres in typical UD composites is seemingly random [3]. However, most geometric algorithms for generating random spatial morphologies are unsuitable for generating RVE's with $V_f \gtrsim 50\%$ [3]. Hence, an in-house UD geometric modelling algorithm, *HEXGenRVE*, was used to generate a hexagonally packed UD RVE for this work.

5.3. Results and discussion of validation exercise

The experimental data alongside predictions from the various PBC enforcement techniques are reported in Tab 2. Furthermore, computational FE contour plots from the different types of periodic BC enforcement techniques are depicted in Figs 10–12.

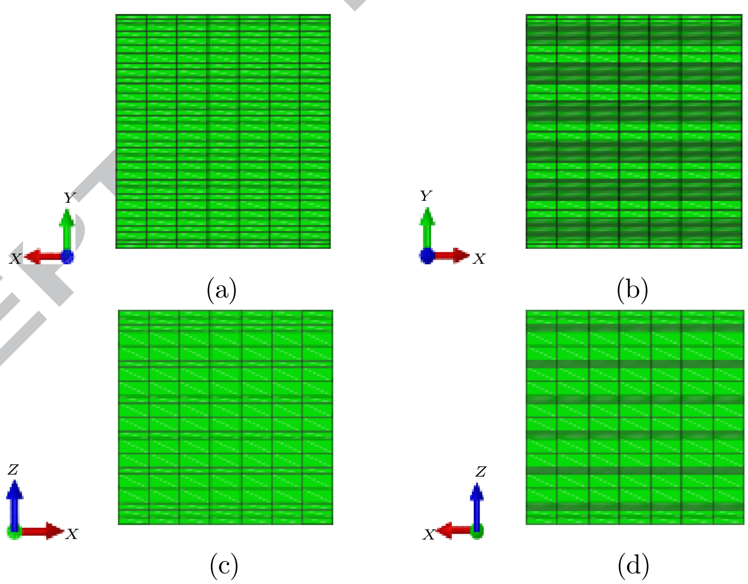

Figure 9: Illustration of the non-homologous mesh of T300/BSL914C (a) $\partial\Omega^{Z-}_{\mathrm{RVE}}$, (b) $\partial\Omega^{Z+}_{\mathrm{RVE}}$, (c) $\partial\Omega^{Y-}_{\mathrm{RVE}}$, and (d) $\partial\Omega^{Y+}_{\mathrm{RVE}}$

For the homologous mesh, predictions from the periodic BC enforcement by kinematic tying and the proposed polynomial interpolation technique coalesce qualitatively and quantitatively.

This coalescence is expected in this special case because for a homologous mesh where the entire nodes on the independent boundary regions are used as the independent degrees of freedom in the interpolation functions, the method reduces to a kinematically tied case periodic BC enforcement. Therefore, the kinematic tying periodic BC enforcement technique is a degenerate form of the proposed polynomial interpolation PBC technique for homologous meshes provided all the entire independent nodal regions of the RVE is used in the interpolation functions. Nevertheless, predictions based on the non-homologous and homologous RVEs equally coalesce qualitatively and quantitatively. Although negligible differences are present within the FE contour plots, these differences stem from inevitable discretisation errors inherent within the RVEs due mesh differences. The similarities between predictions from the homologous and non-homologous mesh is recovered because the proposed PBC enforcement technique by polynomial implementation faithfully reproduces the appropriate boundary constraints on the RVE. Consequently, this induces the exact stress-strain response within the RVE when compared with the PBC enforcement by kinematic tying which is verified by a comparison of the contour plots and deformations generated for the kinematic tying and polynomial interpolation cases (see Figs 10 and 12). Finally, all the predicted effective elastic constants agree excellently with experimental data because appropriate boundary conditions have been enforced. Therefore, this virtual testing technique is well-suited for use in determining a holistic range of effective elastic constants of continuous fibre reinforced composites.

Table 2: Comparison of predicted effective elastic constants of T300/BSL914C ($V_f = 60\,\%$) using different implementations of PBC and experimental data [13].

Elastic constant	Experiment	Homologous mesh: PBC enforcement by kinematic tying	Homologous mesh: PBC enforcement by polynomial interpolation	Non-homologous mesh: PBC enforcement by polynomial interpolation
E_{11} (GPa)	138	133	133	133
E_{22} (GPa)	11	10	10	10
E_{33} (GPa)	11*	10	10	10
ν_{12}	0.28	0.23	0.23	0.23
ν_{13}	0.28*	0.23	0.23	0.23
ν_{23}	0.4	0.37	0.37	0.37
G_{12} (GPa)	5.5	4.2	4.2	4.2
G_{13} (GPa)	5.5*	4.2	4.2	4.2
G_{23} (GPa)	3.9**	3.3	3.3	3.3

* Transverse isotropy in the 2-3 plane is assumed.

** Computed based on transverse isotropy in the 2-3 plane by $G_{23} = \frac{E_{22}}{2(1+\nu_{23})}$.

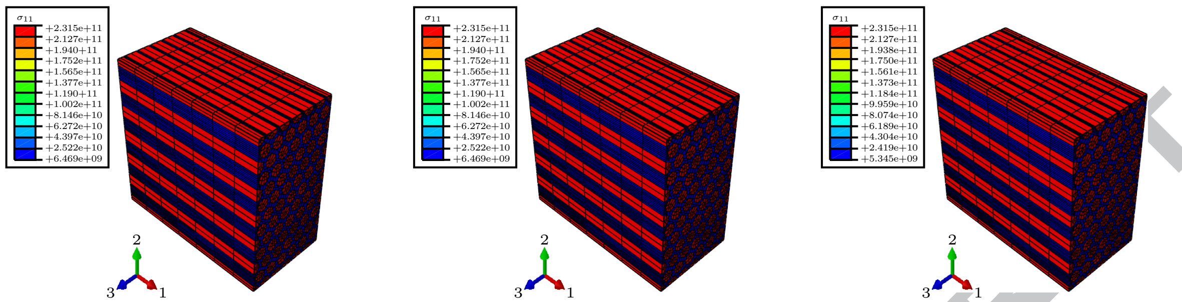

(a) (b) (c)

Figure 10: Comparison of FE contour plots illustrating longitudinal tensile deformation (i.e. ε_{11}) of T300/BSL914C (a) homologous mesh with PBC enforcement by kinematic tying, (b) homologous mesh with PBC enforcement by polynomial interpolation, and (c) non-homologous mesh with PBC enforcement by polynomial interpolation.

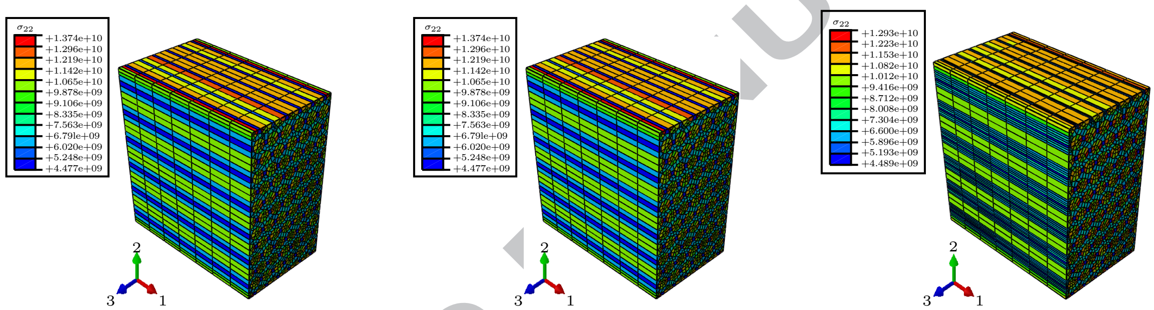

(a) (b) (c)

Figure 11: Comparison of FE von Mises contour plots illustrating transverse tensile deformation (i.e. ε_{22}) of T300/BSL914C (a) homologous mesh with PBC enforcement by kinematic tying, (b) homologous mesh with PBC enforcement by polynomial interpolation, and (c) non-homologous mesh with PBC enforcement by polynomial interpolation.

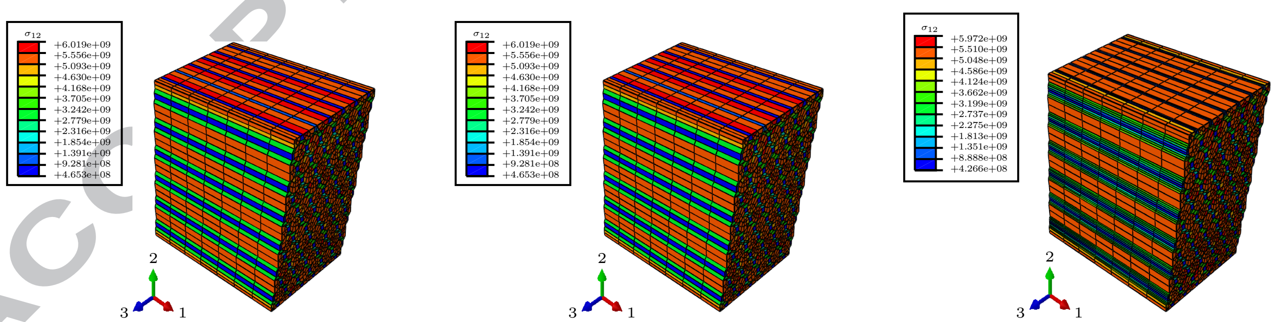

(a) (b) (c)

Figure 12: Comparison of FE contour plots illustrating in-plane shear deformation (i.e. ε_{12}) of T300/BSL914C (a) homologous mesh with PBC enforcement by kinematic tying, (b) homologous mesh with PBC enforcement by polynomial interpolation, and (c) non-homologous mesh with PBC enforcement by polynomial interpolation.

6. Predicting the effective properties of textile composites with an arbitrary FE Mesh

6.1. Test material

Having validated the proposed PBC enforcement technique for arbitrary FE meshes, using a UD composite as a test case, the next step is to use this validated technique to predict the effective elastic properties of textile composites. The selected test material for the prediction analysis is a through-the-thickness angle-interlock composite (TTT-AIC) with low crimp and an epoxy matrix [14]. The mechanical properties of this material are reported in Tab 3. This composite was chosen because experimental data on four, out of the nine independent effective elastic properties, were available. The idealised geometry and geometric parameters of this TTT-AIC are reported in Fig 13 and Tab 4, respectively.

Table 3: Mechanical properties of the constituents of the through-the-thickness angle-interlock textile composite [14].

Elastic constant	Tenax HTA	Tenax HTS	RTM-6 Epoxy
Longitudinal modulus (GPa), E_{11}	240	240	2.84
Transverse modulus (GPa), E_{22}	14	14	2.84
In-plane shear modulus (GPa), G_{12}	20	20	1.029
Transverse shear modulus (GPa), G_{23}	10	10	1.029
Major Poisson's ratio, ν_{12}	0.3	0.3	0.38
Minor Poisson's ratio, ν_{23}	0.39	0.39	0.38

6.2. Textile geometric model generation

An in-house textile composite generating algorithm, *TextCompGen*, was developed and implemented in MATLAB to generate textile RVEs. TextCompGen requires the following input data to generate a textile: (a) Textile fabric type (i.e. TTT-AIC), (b) Number of warp yarn layers, (c) Ratio of warp yarns per layer to the total number of binder yarns within the RVE, (d) Number of weft yarns that a binder yarn passes in the weft layer before reversing its direction, (e) Yarn width, height and spacing of the warp, weft and binder yarns, and (f) Yarn cross-sectional shape (e.g. Ellipse, Lenticular, Racetrack) of the warp, weft and binder yarns. FE-ready replicas of the geometric outputs from TextCompGen are created in ABAQUS/CAE using its native Python scripting commands (Fig 13 was generated using this algorithm).

TextCompGen was designed to capture the principal features of the textile being studied without recourse to modelling all the intricate features commonly observed in textile composites. The principal features which ensure correspondence between the actual textile and geometric model are overall fibre volume fraction, o-V_f, and fabric thickness, H [15]. The overall fibre volume fraction is important because it determines the fabric's areal density, matrix content and specific weight. Whilst the fabric thickness, H, is important because it directly relates to the o-V_f and it governs the through-thickness crimp of fabrics. However, it is difficult to match the experimentally observed

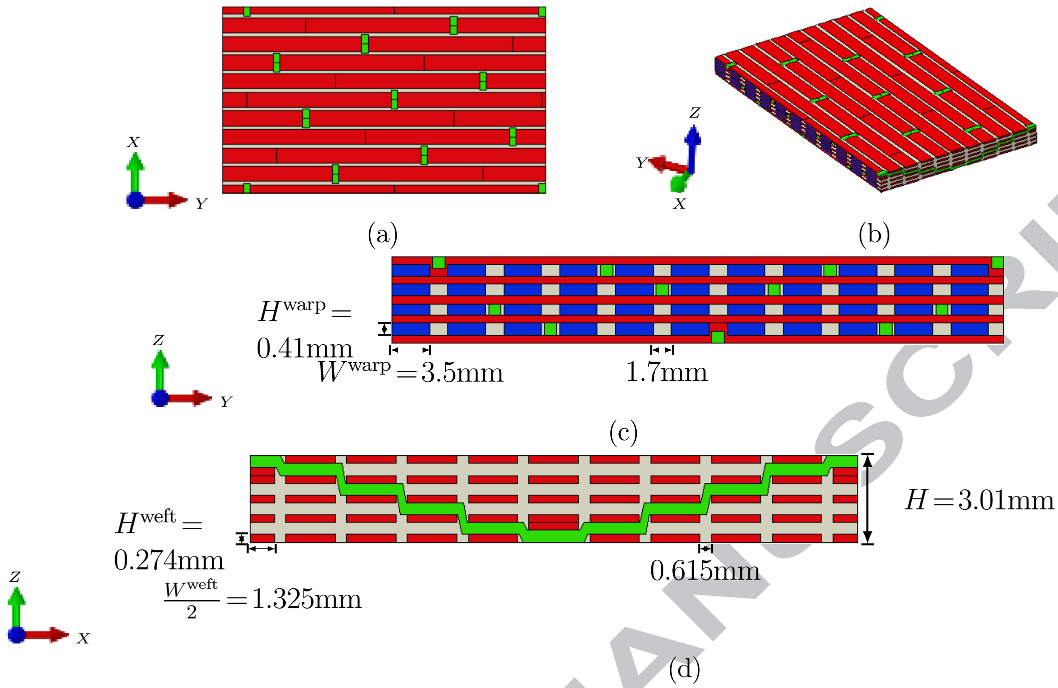

Figure 13: Idealised geometric model of the TTT-AIC fabric: (a) XY plane view, (b) Isometric view, and (c) YZ plane view, and (d) XZ plane view.

and geometrically determined iy-V_f to yield the appropriate o-V_f. Thus, for the geometric models, an interplay between iy-V_f and y-V_f is necessary. Also, within the geometric model, maximum crimp of the surface weft yarns was enforced at the crossover regions between the binder and weft yarns to maintain the experimentally observed fabric thickness. Tab 4 reports a comparison between the geometric parameters/features of the actual and computational TTT-AIC fabric.

Two well-known problems of performing virtual FE tests on consolidated textile composites are (a) discretisation and (b) representative virtual domain size. These problems stem from the characteristic complexities of textile topologies in conjunction with the appreciable size of textile repeating unit cells. Therefore, simplifications were invoked in the textile FE models to facilitate discretisation and improve solution times. To obviate discretisation problems whilst using a desirable hexahedral-dominated conformal mesh, rectangular cross-sections were adopted for the yarns within the TTT-AIC fabric. Furthermore, multiple geometric partitions were introduced within the geometric domain to generate simple cuboidal regions readily amenable to conformal meshing. Finally, only one binder yarn was incorporated within the discretised FE geometric model of the TTT-AIC fabric.

6.3. Textile FE model set-up and homogenisation technique

In analysing the textile composite this study adopted a so-called dual-scale homogenisation method. This method requires analyses at two length-scales: one at the micro-scale and the other at a meso-scale. First the yarns were decomposed into their primary constituents: matrix and fibre.

Table 4: Comparison between the geometric features of the actual and computationally-generated TTT-AIC fabric.

Geometric feature	Actual Textile	Computational Textile
Thickness, H (mm)	3	3.01
Warp intra-yarn volume fraction, iy-V_f^{warp} (%)	64.4	66.4
Warp fibre volume fraction, V_f^{warp} (%)	-	48.5
Weft intra-yarn volume fraction, iy-V_f^{weft} (%)	63.6	65.6
Weft fibre volume fraction, V_f^{weft} (%)	-	47.2
Binder intra-yarn volume fraction, iy-V_f^{binder} (%)	66.3	68.3
Binder fibre volume fraction, V_f^{binder} (%)	6	4.3
Overall fibre volume fraction, o-V_f (%)	51	51
Areal density, ρ^{areal} (g/m^2)	-	4389
Warp cross-sectional shape	[ ]	[ ]
Weft cross-sectional shape	( )	[ ]
Binder cross-sectional shape	( )	[ ]
Surface weft yarn crimp	moderate	extreme

Thereafter, yarns were modelled at the micro-scale as, densely packed, orthotropic UD composites (i.e. an identical analysis technique was used in Section 5). Subsequently, the homogenised effective elastic constants extracted from the micro-scale analysis were used as inputs for the meso-scale continuum model for each yarn as reported in Tab 5. The arbitrary undulation of each yarn was considered by assigning discrete material orientations to each yarn within the fabric. Furthermore, the discrete matrix pockets at the meso-scale are modelled using an identical Hookean elastic model used in the micro-scale analysis. Finally, the homogenised effective elastic material properties extracted from the meso-scale analysis represents the required global material properties.

Table 5: Predicted effective elastic constants of the warp, weft and binder yarns comprising the TTT-AIC.

Elastic constant	Warp yarn	Weft yarn	Binder yarn
E_{11} (GPa)	155	153	160
E_{22} (GPa)	10.1	10.1	10.4
E_{33} (GPa)	10	9.97	10.3
ν_{12}	0.33	0.33	0.33
ν_{13}	0.33	0.33	0.33
ν_{23}	0.32	0.32	0.32
G_{12} (GPa)	4.03	3.98	4.26
G_{13} (GPa)	3.89	3.84	4.13
G_{23} (GPa)	3.6	3.58	3.74

6.4. Results and Discussion

The experimental data alongside predictions from the proposed PBC enforcement technique by polynomial interpolation are reported in Tab 6. Additionally, contour plots of the full-field stress from FE tests are reported in Figs 14–16.

The predicted Youngs modulus along the in-plane material directions (i.e. E_{xx} and E_{yy}) from the virtual test corroborates experimental results. However, the virtual test marginally over-predicts the stiffness in both cases with a predictive discrepancy of about 2 %. This over-prediction may be borne from the regularity of the virtual model in comparison to the geometric variations inherent in the real material. Nevertheless, the current predictive fidelity is superior to those reported in previous work on textile reinforced composites where discrepancies between 10 % to 40 % were reported [16, 17, 18, 19]. A plausible reason for the current high fidelity of the predicted effective material properties, especially in the in-plane material direction, stems from the properly enforced periodic BC on the textile domain as well as the dual-scale homogenisation strategy adopted in this work.

In comparison to experiments, the current virtual test over-predicts the through-the-thickness Young's modulus (i.e. E_{zz}), by about 36 %. This discrepancy is in line with predictions from previous work on similar through-the-thickness reinforced fabric [20]. It is noted, however, that the experimental value for E_{zz} was inferred from a through-thickness compression test which introduces inherent experimental uncertainties of 15 % [20, 21]. Furthermore, the overestimation of E_{zz} by the virtual test most likely stems from the combined assumption that the binder yarn follows a zig-zag path, and the surface weft yarns have maximum crimp. In practice, the binder yarn follows more curved trajectory and therefore possesses a higher undulation in the thickness direction of the fabric. As a result, the reinforcing effect of the binder yarn is not as pronounced as the current geometric model suggests. With respect to the surface weft yarns of the fabric, the maximum crimp enforced within the geometric model allows regions of the textile to experience the full longitudinal load-baring capacity of the weft yarns. Thus, this manifests as an exaggerated stiffness in the through-the-thickness direction of the virtual model In reality, the surface weft yarn experience moderate crimp; therefore, only a fraction of the longitudinal load-bearing capacity of the weft yarns is experienced in the thickness direction of the textile.

There is a 73 % discrepancy between the predicted in-plane shear modulus (i.e. G_{xy}) and the reported experimental data. The principal source of this discrepancy is most likely from the experimental data reported by the originating authors [14]. The authors performed a 45° off-axis tensile test on the TTT-AIC specimen; however, the mandatory data reduction steps necessary for this test method was not reported in their work, casting doubt on its veracity. Previous work on experimental determination of in-plane shear modulus [17] of a similar TTT-AIC fabric reported average values of about 4 GPa. Furthermore, previous work on experimental and virtual characterisation of woven textile composites [21] reported that the shear moduli of these composites are similar to those of its constituent yarns. Hence, results from the current work is qualitatively, and to a large degree, quantitatively consistent with these previous findings on the in-plane shear modulus, (i.e. G_{xy}), of the composite. The predicted magnitudes of the through-thickness shear moduli (i.e. G_{xz} and G_{yz}) are equally similar to that of the in-plane shear modulus (i.e. G_{xy}) of the composite.

More important, the originating authors [14] did not report experimental data for the Poisson's ratio of the composite. However, the current virtual test predicted the entire Poisson's ratios and the reported magnitudes are qualitatively similar to those reported for a comparable woven textile composites [21].

Table 6: Comparison of predicted effective elastic constants of the TTT-AIC textile using the proposed PBC enforcement technique and experimental data [14].

Elastic constants	Experiment	Virtual test
E_{xx} (GPa)	64	65.4
E_{yy} (GPa)	62	62.6
E_{zz} (GPa)	7	9.5
ν_{xy}	-	0.045
ν_{xz}	-	0.370
ν_{yz}	-	0.380
G_{xy} (GPa)	11	2.98
G_{xz} (GPa)	-	3.01
G_{yz} (GPa)	-	3.17

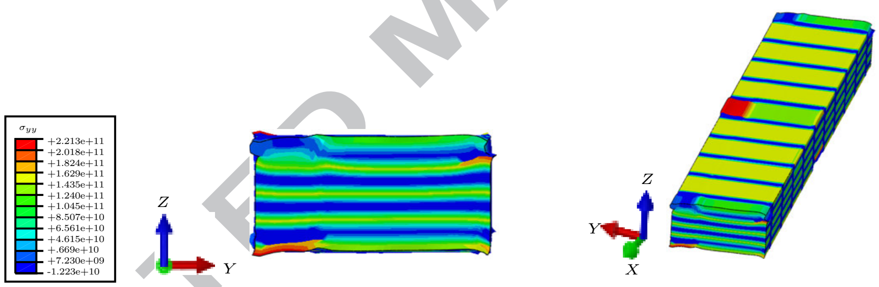

(a) (b)

Figure 14: FE contour plots illustrating tensile deformation of the TTT-AIC along the weft direction (i.e. ε_{yy}) (a) YZ view, and (b) Isometric View.

7. Conclusions

A virtual testing framework for characterising the mechanical response of typical heterogeneous materials with a robust technique for enforcing periodic boundary condition has been presented. Periodic boundary condition is enforced by interpolating the displacement field on the RVE's boundary utilising two piecewise interpolation techniques: (1) cubic Hermite interpolation and, (2) linear triangulation interpolation. A typical RVE in $\mathbb{R}^3$ is properly decomposed into specific regional sets: (1) vertex regional sets, (2) edge regional sets, and (3) internal surface regional sets. Through the judicious use of geometric symmetry, each regional set is decomposed further into independent and dependent regional sets to preclude over-constraints of some node on the RVE's

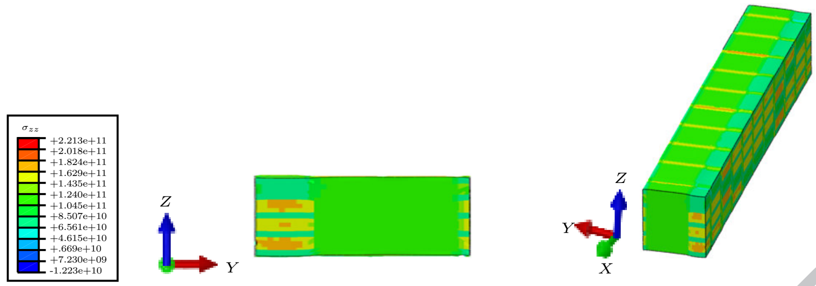

(a) (b)

Figure 15: FE contour plots illustrating tensile deformation of the TTT-AIC along the through-thickness direction (i.e. ε_{zz}) (a) YZ view, and (b) Isometric View.

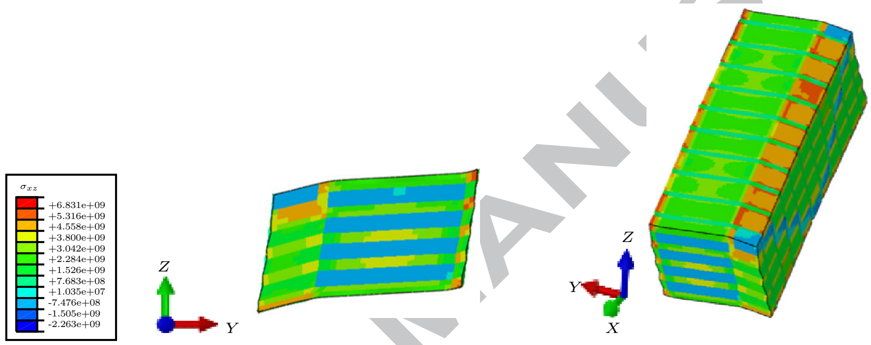

(a) (b)

Figure 16: FE contour plots illustrating through-thickness shear deformation of the TTT-AIC (i.e. ε_{yz}) (a) YZ view, and (b) Isometric view.

boundary. Subsequently, *supplementary nodes* are introduced into the FE problem which provide leverage to introduce constants for the interpolation functions and macroscopic strain tensor, using multi-point constraint equations. The cubic Hermite and linear triangulation interpolants are used to interpolate the displacement field of the RVE's edges internal surface regions, respectively. A principal advantage of this periodic boundary condition enforcement technique is its applicability to an arbitrary FE mesh design: homologous or non-homologous. Therefore, it allows a flexible FE mesh design, especially for heterogeneous materials with complex geometric architectures such as textile composite, where homologous mesh designs are infeasible.

To validate the veracity of the proposed periodic boundary condition enforcement technique, a unidirectional composite with readily controllable mesh design was analysed. Homologous and non-homologous mesh designs of the UD composite were analysed. For the homologous mesh design, a conventional technique using kinematic tying and the proposed interpolation technique were used to enforce periodic boundary conditions. Virtual tests showed that both techniques produced identical stress-strain fields and homogenised responses within the RVE. Whereas for the non-homologous mesh design, only the periodic boundary condition enforcement by interpolation was applicable. In this case, results showed that this technique produced similar stress-strain fields and homogenised responses within the RVE in comparison to the homologous mesh case, barring negligible FE discretisation errors. Thus, in the case of a homologous mesh design the classic kinematic tying technique of enforcing periodic boundary condition is a degenerate case of the interpolation technique discussed in this study; consequently, the interpolation technique is a superior technique for enforcing periodic boundary conditions because of its additional applicability to non-homologous meshes.

Subsequent tests on a through-the-thickness angle interlock textile composite with a complex architecture, and consequently non-homologous mesh, produced results which were corroborated experimental data. Given the limitations of computational power and virtual geometric sizes, the current method is more accurate than the enforcement of Dirichlet boundary conditions which is usually considered for complex architectures with non-homologous meshes. Moreover, the current technique does not appreciably increase computational expenses because only a limited number of additional degrees of freedom are introduced in the FE problem. Thus, the analysis presented herein can be extended to more sophisticated aspects of heterogeneous material behaviour particularly for non-linear finite deformation.

References

[1] B. Farahmand, Virtual Testing and Predictive Modeling: for Fatigue and Fracture Mechanics Allowables, Springer, New York, USA, 2009.

[2] M. I. Okereke, A. I. Akpoyomare, M. S. Bingley, Virtual testing of advanced composites, cellular materials and biomaterials: A review, Composites Part B: Engineering 60 (2014) 637–662.

[3] M. I. Okereke, A. I. Akpoyomare, A virtual framework for prediction of full-field elastic response of unidirectional composites, Computational Materials Science 70 (null) (2013) 82–99.

[4] V.-D. Nguyen, E. Béchet, C. Geuzaine, L. Noels, Imposing periodic boundary condition on arbitrary meshes by polynomial interpolation, Computational Materials Science 55 (2012) 390–406.

[5] S. V. Lomov, D. Ivanov, I. Verpoest, M. Zako, T. Kurashiki, H. Nakai, S. Hirosawa, Meso-FE modelling of textile composites: Road map, data flow and algorithms, Composites Science and Technology 67 (9) (2007) 1870–1891.

[6] S. Jacques, I. De Baere, W. Van Paepegem, Application of periodic boundary conditions on multiple part finite element meshes for the meso-scale homogenization of textile fabric composites, Composites Science and Technology 92 (2014) 41–54.

[7] M. Y. Matveev, A. C. Long, I. A. Jones, Modelling of textile composites with fibre strength variability, Composites Science and Technology 105 (2014) 44–50.

[8] A. S. Koumpias, K. I. Tserpes, S. Pantelakis, Progressive damage modelling of 3D fully interlaced woven composite materials, Fatigue & Fracture of Engineering Materials & Structures 37 (7) (2014) 696–706.

[9] J. M. Tyrus, M. Gosz, E. DeSantiago, A local finite element implementation for imposing periodic boundary conditions on composite micromechanical models, International Journal of Solids and Structures 44 (9) (2007) 2972–2989.

[10] J. C. Michel, H. Moulinec, P. Suquet, Effective properties of composite materials with periodic microstructure: a computational approach, Computer Methods in Applied Mechanics and Engineering 172 (1-4) (1999) 109–143.

[11] I. Amidror, Scattered data interpolation methods for electronic imaging systems: a survey, Journal of Electronic Imaging 11 (2) (2002) 157.

[12] M. Danielsson, D. M. Parks, M. C. Boyce.

[13] M. J. Hinton, A. S. Kaddour, P. D. Soden, Failure Criteria in Fibre Reinforced Polymer Composites: The World-Wide Failure Exercise, Elsevier, 2006.

[14] R. Gerlach, C. R. Siviour, J. Wiegand, N. Petrinic, In-plane and through-thickness properties, failure modes, damage and delamination in 3D woven carbon fibre composites subjected to impact loading, Composites Science and Technology 72 (3) (2012) 397–411.

[15] D. S. Ivanov, S. V. Lomov, 2 - Modelling the structure and behaviour of 2D and 3D woven composites used in aerospace applications, in: P. E. Irving, C. Soutis (Eds.), Polymer Composites in the Aerospace Industry, Woodhead Publishing, 2015, pp. 21–52.
[16] F. Stig, S. Hallström, A modelling framework for composites containing 3D reinforcement, Composite Structures 94 (9) (2012) 2895–2901.
[17] S. Buchanan, E. Archer, D. Townsend, S. Jenkins, A. McIlhagger, J. Quinn, Determination of in-plane shear modulus of 3D woven composites with large repeat unit cells, Plastics, Rubber and Composites 41 (4) (2012) 194–198.
[18] X. F. W. Wang, X. F. W. Wang, G. M. Zhou, C. W. Zhou, Multi-scale Analyses of 3D Woven Composite Based On Periodicity Boundary Conditions, Journal of Composite Materials 41 (14) (2007) 1773–1788.
[19] Z. Wu, Three-dimensional exact modeling of geometric and mechanical properties of woven composites, Acta Mechanica Solida Sinica 22 (5) (2009) 479–486.
[20] S. Buchanan, A. Grigorash, E. Archer, A. McIlhagger, J. Quinn, G. Stewart, Analytical elastic stiffness model for 3D woven orthogonal interlock composites, Composites Science and Technology 70 (11) (2010) 1597–1604.
[21] B. N. Cox, M. S. Dadkhah, The Macroscopic Elasticity of 3D Woven Composites, Journal of Composite Materials 29 (6) (1995) 785–819.